Zhu Jialei (Orcid ID: 0000-0003-2057-8996)
Penner Joyce, E. (Orcid ID: 0000-0001-5577-452X)

Indirect effects of secondary organic aerosol on cirrus clouds

Jialei Zhu[1,2] and Joyce E. Penner[2]

1 Institute of Surface-Earth System Science, Tianjin University, Tianjin 300072, China

2 Department of Climate and Space Sciences and Engineering, University of Michigan, Ann Arbor, Michigan 48109, USA

Corresponding Author: Jialei Zhu (Email: zhujialei@tju.edu.cn)

Key Points:

- The radiative effect of SOA is estimated to be 0.31 to 0.35 W m^{-2} using assumed and predicted size distributions
- The radiative forcing of aircraft soot is decreased from -0.2 W m^{-2} to -0.11 W m^{-2} when SOA acting as an INP is added to the background atmosphere

This is the author manuscript accepted for publication and has undergone full peer review but has not been through the copyediting, typesetting, pagination and proofreading process, which may lead to differences between this version and the Version of Record. Please cite this article as doi: 10.1029/2019JD032233

- The historical radiative forcing of SOA on cirrus clouds is estimated to be 0.02±0.04 W m^{-2} with the predicted SOA size distribution

Abstract

Secondary organic aerosols (SOA) have been identified as a potential source of depositional ice nucleating particles and thus may have a radiative effect on cirrus clouds. This study develops a global model to examine the radiative effect of SOA in cirrus clouds using different treatments for the size distribution of SOA. The SOA from new particle formation by organics and their subsequent growth has a radiative effect of 0.35±0.06 W m^{-2}, while the radiative effect of SOA calculated by assuming a fixed size distribution is 0.31±0.08 W m^{-2}. This positive radiative effect on cirrus clouds opposes the negative effect of anthropogenic soot on cirrus clouds. In addition, the inclusion of SOA as an ice nucleating particle changes the background ice crystal number concentration which impacts the calculation of radiative forcing from other aerosols. The radiative forcing of aircraft soot is estimated to be -0.11±0.03 W m^{-2} when including SOA formed from new particle formation by organics and growth. This is less negative than simulations that do not include ice nucleation from SOA. The change in SOA formed from organic nucleation from the preindustrial period to the present day causes a positive forcing of 0.02±0.04 W m^{-2}. It is important to use a size

distribution based on the explicit formation mechanism for SOA to calculate their radiative effects. The simulation using an assumed fixed size distribution incorrectly results in a negative forcing of SOA between the present day and pre-industrial atmospheres because it does not correctly calculate the change of SOA in the accumulation mode.

1. Introduction

Cirrus clouds play an important role in the Earth's radiation budget. Homogeneous freezing of sulfate haze particles and heterogeneous nucleation triggered by insoluble ice nucleating particles (INPs) like dust and soot have been regarded as important contributors to ice nucleation processes, and thus influence cirrus cloud cover and optical properties [*Hoose and Möhler*, 2012; *Koop et al.*, 2000; *Koop et al.*, 1998]. However, the radiative effects of glassy secondary organic aerosols (SOA) on cirrus clouds have not received a large amount of attention, although SOA are ubiquitous and abundant in the atmosphere and have the potential to act as heterogeneous INP if they become glassy [*Knopf et al.*, 2018; *Murray et al.*, 2010].

SOA forms as a result of gaseous and aqueous reactions of biogenic and anthropogenic sources of volatile organic compounds (VOCs). The mechanism of SOA formation determines its size distribution and mixing with other aerosol types, so it also determines its radiative effects [*Zhu et al.*, 2017]. The formation mechanism results in SOA that is internally mixed with other particles, consistent with measurements that indicate that most carbonaceous particles are

internally mixed with other aerosols in both polluted and remote areas, and at all altitudes [*Cahill et al.*, 2012; *Pratt and Prather*, 2010]. Thus, it is not appropriate to treat sulfate and SOA particles as externally mixed as in many previous simulations [*Penner et al.*, 2018; *Satheesh and Moorthy*, 2005; *Zhou et al.*, 2016]. Previous simulations showed that most of the predicted SOA is mixed with sulfate aerosols [*Zhu et al.*, 2017].

Recently, some highly oxygenated molecules (HOMs) with low volatility were found to be able to form new organic particles via heteromolecular nucleation of sulfuric acid and organics as well as by pure organic nucleation in experiments in the CLOUD (Cosmics Leaving Outdoor Droplets) project [*Kirkby et al.*, 2016; *Riccobono et al.*, 2014]. As a result, new SOA particles can form when sulfuric acid concentrations are low and/or in the absence of sulfuric acid, so SOA is expected to be a potentially widespread source of new particles in the preindustrial atmosphere [*Gordon et al.*, 2016; *Zhu et al.*, 2019]. Inclusion of these organic nucleation processes radically alters the number concentration and size distribution of SOA particles over the world, [*Zhu et al.*, 2019]. Based on these results, it is important to

examine how cirrus cloud formation is altered by SOA to determine their importance to climate based on the mechanism of SOA formation.

Many experiments have shown that some SOA compounds exhibit a highly viscous semisolid or even glassy state at low temperatures and low relative humidity [*Koop et al.*, 2011; *Pajunoja et al.*, 2014; *Renbaum-Wolff et al.*, 2013; *Saukko et al.*, 2012]. If glassy SOA particles are present at conditions conductive to ice formation, they could potentially serve as heterogeneous INP via immersion, contact and depositional freezing modes [*Knopf et al.*, 2018]. Organic materials are widely found in the ice crystal residues of cirrus clouds [*Chen et al.*, 1998; *Cziczo et al.*, 2013; *DeMott et al.*, 2003; *Froyd et al.*, 2010]. *Ignatius et al.* [2016] and *Wagner et al.* [2017] observed heterogeneous ice nucleation of viscous α-pinene SOA for ice saturation ratios of 1.3~1.4 and temperatures 205K~253K. *Wilson et al.* [2012] found that SOA particles are able to nucleate ice heterogeneously at tropical tropopause levels. Modelling studies also predict that SOA particles are efficient INPs under cirrus conditions in the upper troposphere since the SOA particles are in a glassy phase state under these conditions [*Berkemeier et al.*, 2014; *Koop et al.*, 2011]. *Baustian et al.* [2013] find that organic

aerosols could be glassy over more than 60% of the time in the midlatitude upper troposphere and more than 40% of the time in the tropical tropopause region. The evaluation of the phase state of SOA by models indicates that most of the SOA particles are glassy above 500hPa (~5 km) [*Shiraiwa et al.*, 2017]. In heterogeneous ice nucleation, the size of the particles also typically plays an important role, so that larger particles tend to be more efficient INPs [*Welti et al.*, 2009].

Ice nucleation in cirrus clouds occurs either homogeneously or heterogeneously. These mechanisms compete to determine the ice crystal number concentration. The number and size of ice crystals impacts the ice water path, cloud cover, lifetime and optical properties of cirrus clouds and thus determines their radiative properties. Homogeneous ice nucleation of supercooled aqueous solutions like sulfate haze particles always requires high relative humidity with respect to ice (RHi) [*Koop et al.*, 2000], while heterogeneous ice nucleation can occur at a lower RHi [*Hoose and Möhler*, 2012]. As a result, heterogeneous nucleation is able to occur in advance of homogeneous nucleation in a rising air parcel. Newly formed ice crystals from heterogeneous nucleation can inhibit homogeneous nucleation as a result of the deposition and consumption of

water vapor, and, since the number concentrations of heterogeneous ice nucleating particles are smaller than those that freeze homogeneously, would lead to a decrease of ice crystal number concentrations if added to regions dominated by homogeneous nucleation [*DeMott et al.*, 2010; *Kärcher and Ström*, 2003; *Spichtinger and Cziczo*, 2010]. In addition, smaller ice crystal number concentrations lead to larger ice crystals compared to cases with only homogeneous nucleation [*Abbatt et al.*, 2006]. On the other hand, the addition of heterogeneous nucleation can also contribute to an increase in ice crystal number concentrations and a decrease in ice crystal size [*Zhao et al.*, 2019], if added to regions that are dominated by heterogeneous nucleation. Therefore, the radiative effect of aerosols on cirrus clouds could differ in both magnitude and sign depending on the competition between these two ice nucleation processes, which is determined by both the number of homogeneous and heterogeneous INPs as well as the updraft or cooling rate [*Zhou and Penner*, 2014]. Based on these results, additional INPs formed from SOA can change the ice crystal number as well as the radiative effects of cirrus clouds.

In this study, INPs from SOA are included in an Earth system model to examine their radiative effects on cirrus clouds. The use of SOA particles with a fixed size distribution (as in previous studies) as well as a scheme that includes the nucleation of new SOA particles from organic gases are compared. We estimate the radiative effect of newly formed SOA particles on cirrus clouds using a treatment of the size distribution for SOA based on its mechanistic formation. We compare these results with results based on using an assumed size distribution for SOA. In addition, the influence of the inclusion of SOA as an INP on the estimation of the radiative effects of aircraft soot on cirrus clouds is assessed.

2. Model and experiments

We used the Community Earth System model (CESM) version 1.2.2 coupled to the University of Michigan IMPACT aerosol model with a resolution of 1.9°×2.5° to simulate aerosols and their effects on cirrus clouds. Seventeen non-SOA aerosol species/types are simulated in the IMPACT model, including sulfate (as sulfuric acid) formed from nucleation and followed in three modes (i.e. nucleation (<5 nm), Aitken

(5-50 nm) and accumulation (>50 nm)), soot from biomass burning (bSoot, i.e., primary organic aerosol and black carbon from biomass burning, which are assumed to be internally mixed), soot from fossil fuel and biofuel burning (fSoot, i.e., primary organic carbon and its associated black carbon) which is followed in three modes based on the number of monolayers of sulfate (assumed uniform) on its surface, aircraft soot in two modes (pre-activated in contrails or not), and dust and sea salt, the latter two of which are each carried in four separate bins with varying radii [*Wang and Penner*, 2010]. The size distributions of soot, dust and sea salt are listed in Table 1 in *Penner et al.* [2018]. In addition to the seventeen aerosol species/types, the model was improved to enable it to read in the total mass and number concentration of SOA predicted in the accumulation mode by a separate version of the IMPACT model, which will be introduced in the following paragraph. New sulfate particles (H_2SO_4) that nucleate and grow to the Aitken and accumulation mode sizes participate in homogeneous nucleation to form new ice crystals. Ammonium sulfate $(NH_4)_2SO_4$ is not included in the model. Dust with fewer than 3 monolayers of sulfate coating are used to form heterogeneous INP in the model. This treatment is consistent with the

results of field studies by *DeMott et al.* [2003], *Cziczo et al.* [2004] and *Richardson et al.* [2007]. 0.05% of fSoot with <1 monolayers of sulfate and 0.1% of fSoot with 1-3 monolayers of sulfate act as INP. These choices are based on the laboratory study by *Koehler et al.* [2009]. 0.1% of bSoot are assumed to be effective INPs based on the field study of *K Pratt et al.* [2011]. Aircraft soot which has previously formed a contrail and has less than 3 monolayers of sulfate is assumed to be an INP, similar to the treatment in *Zhou and Penner* [2014]. The aerosols simulated by the IMPACT model only interact with the physical processes that form cirrus clouds in the CESM model.

Our parameterization of ice particle nucleation uses a modified version of the air parcel parameterization developed by *Kärcher et al.* [2006]. This parameterization uses a simplified adiabatic parcel model to calculate the supersaturation (S_i) as a function of the updraft and aerosol concentrations at each grid. S_i is updated every second using

$$\frac{dS_i}{dt} = a_1 S_i w - (a_2 + a_3 S_i) \int_0^\infty dr_0 \frac{dn}{dr_0} R_{im}(r_0)$$

where the parameter a_1 is given by $a_1 = (L_s M_w g)/(c_p R T^2) - Mg/(RT)$, with the molar mass of air M and water M_w, latent heat of

sublimation L_s, constant of gravity g, heat capacity at constant pressure c_p, the universal gas constant R, and air temperature T. w is the vertical velocity. a_2=1/n_{sat} with the water vapor number density at ice saturation n_{sat}. $a_3 = L_s^2 M_w m_w/(c_p pTM)$, with the mass of a water molecule m_w and the air pressure p. R_{im} is the monodisperse freezing/growth integral,

$$R_{im} = \frac{4\pi}{v}\int_{-\infty}^{t} dt_0 \dot{n}_i(t_0) r_i^2(t_0, t)\frac{dr_i}{dt}(t_0, t),$$

where v is the specific volume of a water molecule. $dt_0\dot{n}_i(t_0)$ is the number density of aerosol particles that nucleate ice and freeze within the time interval between t_0 and $t_0 + dt_0$, $r_i(t_0, t)$ is the radius of the spherical ice particle at time t that froze and commenced to grow at time $t < t_0$, and dr_i/dt is the radial growth rate of that ice particle.

A series of updraft and downdraft velocities is used to determine the maximum RHi and the number of ice crystals that nucleate based on the treatment in *Penner et al.* [2018]. The updraft velocities at each grid point are estimated using the combined observations in *Podglajen et al.* [2016] and *Gary* [2006; 2008]. The other processes which influence the microphysics of cirrus clouds including detrainment, the Bergeron process, melting of ice, freezing of cloud drops, autoconversion from ice to snow, growth and sublimation of ice, and sedimentation of ice are

based on *Morrison and Gettelman* [2008] and *Gettelman et al.* [2010]. The detailed model description and setup can be found in *Penner et al.* [2018].

We set up seven simulations using different assumptions for the number of background heterogeneous INP. The BASE case (dbfc) only includes dust, bSoot, fSoot and contrail-processed aircraft soot as heterogeneous INP. The other six sensitivity cases all include SOA as heterogeneous INP, which are classified into two groups based on two different SOA schemes. Soot (i.e., aircraft, fSoot, and bSoot) as well as SOA were set to activate at an RHi of 135% while dust activates at 120%. The ice nucleation parameterization from *Kärcher et al.* [2006] accounts for the continuous competition between homogeneous and heterogeneous nucleation at any given temperature and allows homogeneous nucleation to occur in the rising parcel even if heterogeneous nucleation has already occurred as long as the supersaturation in the parcel reaches the limits set by *Koop et al.* [1998]. In the Kärcher et al. (2006) parameterization, each type of INP is divided into 30 size bins. The ice nucleation scheme calculates the nucleation of INPs from the largest size bin to smallest size bin when the supersaturation is above the threshold (135% for soot and

SOA and 120% for dust). If the required ice amount (w_I in molecules of water m^{-3}) that is calculated to nucleate for all INPs is less than the maximum instantaneous ice amount, determined by $w_I = a_1 \times S_i/(a_2 + a_3 \times S_i) \times w$ then all INPs form ice crystals. If not, the maximum allowed ice amount determines the fraction of INPs that form ice crystals.

The first SOA scheme (used in the dbfcs_fix, dbfs_fix and dbfcs_PI_fix cases in Table 1) reads in the mass concentration of total SOA and computes the number concentration assuming a log-normal size distribution with a mode radius of 0.07 μm and a geometric standard deviation of 1.5 [*Pusechel et al.*, 1992]. This is the same as the method as used by *Penner et al.* [2018] and has a global average burden of SOA of 1.9 mg m^{-2}. The SOA mass concentration was simulated using the IMPACT model with the anthropogenic emissions in 2000 adopted from those used in Community Atmosphere Model (CAM) with Chemistry [*Lamarque et al.*, 2012]. The mass of SOA was formed from volatile organic carbon (VOC) emissions using both an explicit gas-phase and aqueous-phase chemical mechanism, but the scheme does not include the prediction of the SOA size distribution. The gas-phase chemical mechanism for the formation of semivolatile organic products includes

the oxidation of isoprene, α-pinene and aromatics [*Lin et al.*, 2012]. The aqueous-phase reactions include glyoxal and methyglyoxal reactions within drops and the kinetic uptake of IEPOX, glyoxal, and methylgloxal on aqueous aerosols [*Lin et al.*, 2014]. Since only the SOA mass is predicted, an assumed size is used for the parcel model parameterization. We used equations 3 and 4 in *Wang et al.* [2012] to determine the glass transition temperature and RHi for ice nucleation for SOA. The upper limit of the glass transition temperature (T_g) was determined using

$$T_g = \frac{w_W T_{g,W} + w_{SOA} T_g / k_{GT}}{w_W + w_{SOA}/k_{GT}}$$

where w_W and w_{SOA} are the mass fractions of water and SOA, respectively, $T_{g,W}$ is the T_g at 136 K for pure water, k_{GT} is the Gordon-Taylor constant for the specific water/organic system. The upper limit of the glass transition RH was determined using

$$RH = \left(1 + \kappa_{SOA} \frac{\rho_W}{\rho_{SOA}} \frac{w_{SOA}}{w_W}\right)^{-1}$$

where κ_{SOA} is the CCN-derived hygroscopicity parameter for SOA, and ρ_w and ρ_{SOA} are the density of water and SOA, respectively.

Richardson et al. [2007] measured the chemical composition of single particles (using NOAA's Particle Analysis by Laser Mass Spectrometry (PALMS)) in the ambient atmosphere as well as the composition of single ice crystal residuals (i.e. INPs) downstream of the Colorado State University Continuous Flow Diffusion Chamber (CFDC) during the second Ice Nuclei Spectroscopy (INSPECT-II) campaign. They characterized the fractional composition of INPs as well as that of both the total ambient particles and the ambient particles with D>0.6 μm (see Figure 5 in *Richardson et al.* [2007]). The fraction of ambient particles that were organics/sulfates was roughly 75% for both size cutoffs, while the fraction of INPs that were organics/sulfates was approximately 33%. Only a small number of the total ambient number concentrations are INPs (of order 10^{-4} of the total ambient number, see Figure 4 in Richardson et al. [2007]), and within those numbers the fraction that is dust as well as the fraction that are metallic particles were greatly enhanced compared to those fractions that are dust and metallic particles in the ambient particles. However, we wanted to use a large fraction of the SOA in our model simulations in order to examine the largest possible impact, so we assumed that 30% of the SOA particles

which are transformed to a glassy state are able to activate as INPs in the _fix schemes. This fraction amounts to about 1% of the total ambient particles during the time and place of the INSPEC-II campaign, so it is larger than that measured by *Richardson et al.* [2007]. Of course, this assumed ratio is highly uncertain and should be updated when future experimental studies become available. Lower assumed fractional activation could lead to a lower number concentration of ice crystals from SOA. However, the effect of lower INPs from SOA on cirrus clouds also depends on the competition between homogeneous and heterogeneous nucleation.

For the 2nd SOA scheme (used in the dbfcs_new, dbfs_new and dbfcs_PI_new cases in Table 1), we extended the chemical mechanism for the oxidation of α-pinene to simulate the formation of HOMs and organic particle nucleation [*Zhu et al.*, 2019]. In this scheme newSOA follows the number concentration of SOA nucleated from highly oxygenated organic molecules (HOMs). Four different HOMs that have been identified to nucleate new particles based on experimental evidence and quantum chemistry calculations (i.e. diacyl peroxide, pinic acid, pinanediol and the oxidation product of pinanediol) are assumed to

nucleate to form new SOA particles. Three organic nucleation schemes are included based on the experimental results of *Kirkby et al.* [2016] and *Riccobono et al.* [2014], which include heterogeneous nucleation of sulfuric acid and HOMs, pure neutral organic nucleation, and ion-induced organic nucleation. Semi-volatile organic compounds (SVOC) and low-volatility products formed from isoprene epoxydiol (IEPOX), glyoxal and methylglyoxal as well as sulfate contribute to the growth of initial newSOA after nucleation. The number concentration of accumulation mode SOA from this version of the IMPACT model is read in to the version used to simulate cirrus ice formation. The burden of newSOA in the accumulation mode is 0.15 mg m^{-2}, which is 8% of total burden of SOA in the 1st SOA scheme. In this scheme, the newSOA in the accumulation mode that meets the requirements of the glass transition temperature and RHi calculated using the method outlined above are able to form new ice particles as heterogeneous INP.

Biomass burning emissions were estimated based on *van der Werf et al.* [2006] and the injection height of emissions were specified following *Dentener et al.* [2006], which varies by ecosystem from the surface to about 6 km. The biomass burning emissions were distributed to

the model level according to the injection height. The emission of dust uses the scheme from *Zender et al.* [2003]. The emission of sea salt uses the scheme from *Mårtensson et al.* [2003] when the dry particle diameter < 2.8 μm and the scheme from *Gong et al.* [1997] when dry particle diameter > 2.8 μm. The chemical mechanisms used in the model are described in *Lin et al.* [2012], *Lin et al.* [2014] and *Zhu et al.* [2019]. The simulated aerosol mass and number concentration were evaluated by comparison with both surface and vertical measurements in our previous publications [*Lin et al.*, 2012; *Lin et al.*, 2014; *Zhu and Penner*, 2019; *Zhu et al.*, 2019].

The dbfcs_fix and dbfcs_new cases include the fossil/bio fuel, biomass burning, and contrail-processed soot INPs that are part of the BASE case (dbfc) and additional INP from SOA using the two schemes described above. In order to assess the influence of INPs from SOA on the estimation of the radiative forcing of aircraft soot on cirrus clouds, we ran the following cases: dbfs_fix and dbfs_new, which are same as dbfcs_fix and dbfcs_new, respectively, but without the INPs from contrail-processed aircraft soot. The difference of the two simulations with and without contrail-processed aircraft soot determines the radiative

forcing of aircraft soot in cirrus clouds. In order to estimate the historical radiative forcing of SOA on cirrus clouds, we ran the cases: dbfcs_PI_fix and dbfcs_PI_new. The dbfcs_PI_fix case is same as dbfcs_fix but reads in the mass concentration of SOA in the pre-industrial (PI) atmosphere as determined in *Zhu et al.* [2019]. The calculation of pre-industrial SOA accounts for the change in biogenic emissions as a result of the temperature increase since 1750 as well as the changes in land-use since 1850. The dbfcs_PI_new case is same as dbfcs_fix but reads in the number concentration of SOA in the accumulation mode in the PI atmosphere. Table 1 provides a summary of these experiments. All cases were run with winds nudged towards ECMWF reanalysis data using a nudging time of 6 hours for the years 2005-2011 [*Zhang et al.*, 2014]. The data for the last six years were used for analysis in this study.

3. Results

3.1 Impact on ice nucleation

In our scheme, the number of SOA particles that act as INPs depends on the mechanism of SOA formation and its glass transition temperature. The spatial and vertical distribution of INPs from SOA in

the two schemes described in Section 2 differ greatly as shown in Figure 1. The fraction of SOA particles in the _new schemes that become glassy is of order 10^{-4} due to the large number of SOA particles that form as a result of nucleation. As a result, in the _new schemes, only a few of SOA particles can transform to a glassy state based on the equations from *Wang et al.* [2012]. In total, the fraction of SOA that may activate as INPs in the _new schemes are of order 10^{-4}. This is roughly similar to the fraction that nucleate in the *Richardson et al.* [2007] field campaign data. The number concentration in the scheme with a fixed size distribution (s_fix) is 81% smaller than that in the scheme using the calculated size distribution with organic nucleation (s_new) while the fraction that form ice crystals is roughly 20-30% (see Table 1 in *Penner et al.* [2018]).

With the fixed size distribution, the number concentration of INPs from SOA has a maximum over the Amazon because of the large emissions of biogenic volatile organic compounds (BVOCs) there (Figure 1c). The peak in the vertical profile occurs in the tropics in the Southern Hemisphere (SH) between 500hPa and 200hPa (Figure 1d), which is primarily determined by the INPs in the upper troposphere over the Amazon. In comparison, the number concentration of SOA in the s_new

scheme is generated from organic nucleation and growth to the accumulation mode. The number concentration of newSOA in the accumulation mode in the Northern Hemisphere (NH) is higher than that in SH since the high concentration of sulfuric acid and VOCs in the NH aids in the growth of newSOA from nucleation mode particles to the accumulation mode [*Zhu et al.*, 2019] (Figure 1a). The lack of sulfuric acid in the tropics and the high number concentration of newSOA at small sizes, make it hard to grow particles to the accumulation mode, which leads to a peak in the number concentration of INP from SOA in the upper troposphere of the NH (Figure 1b). SOA particles are distributed all over the world even over Antarctica. The SOA particles over Antarctica are formed from the BVOC emitted in the South Hemisphere (mainly in the tropics). SOA is transported and removed by precipitation after its formation resulting in the smaller concentrations over Antarctica compared to values further north.

INPs from SOA are able to preclude homogeneous nucleation due to the consumption of available water vapor before homogeneous nucleation occurs, thereby reducing the ice crystal number concentration (Ni). However, INPs are also able to increase Ni if they are introduced in

regions where heterogeneous nucleation dominates. Figure 2 shows the fraction of zonal average ice crystals formed from homogeneous nucleation in each case and the differences with and without SOA as an INP. In the BASE case (dbfc), homogeneous nucleation dominates in the upper troposphere in the tropics and SH, while in the NH heterogeneous nucleation dominates. The INPs from SOA in both sensitivity cases (dbfcs_fix and dbfcs_new) reduce the fraction of ice crystals from homogeneous nucleation in the tropics and SH with the largest change occurring around 100 hPa, while the INPs from SOA only change the fraction by a small amount in the NH (Figure 2d, e). Many regions in the SH which were dominated by homogeneous nucleation change to regions that are dominated by heterogeneous nucleation in the dbfcs_new simulation. The change in dbfcs_new is considerably larger than the change introduced by dbfcs_fix. The global annual average vertically integrated Ni from homogeneous nucleation is decreased by 23×10^7 m^{-2} (from 117×10^7 m^{-2} in the BASE case) due to the INPs from SOA in the dbfcs_new case, while it is decreased by 16×10^7 m^{-2} for the dbfcs_fix case (Figure 3a, 3b). The largest changes occur over the tropics and Antarctica where Ni are high in the BASE case. Simultaneously, the INPs

from SOA also increase the vertically integrated Ni from heterogeneous nucleation by 24×10^7 m^{-2} and 10×10^7 m^{-2} in the dbfcs_new and dbfcs_fix cases, respectively (Figure 3c, 3d). However, even with these changes, the contribution of homogeneous nucleation still dominates the global average concentration of newly formed ice crystals (Figure 2b, 2c) with the 52% and 63% of ice crystals from homogeneous nucleation in dbfcs_new and dbfcs_fix cases, respectively.

The changes of total Ni depend on the net change as a result of increases and decreases of Ni from the addition of heterogeneous INPs as shown in the Figure 4a, 4b. The INPs from SOA decrease Ni in most tropical regions and Antarctica in the dbfcs_fix case. They only increase the Ni in the Amazon and some ocean regions in the SH. The global average Ni is decreased by 5.5×10^7 m^{-2} by INPs from SOA in the dbfcs_fix case. In comparison, the INPs from SOA in the dbfcs_new case increase Ni in the tropical Indian Ocean and Antarctica. When INPs from SOA are added to the model, the number of Ni produced from homogeneous freezing decreases. Although INPs from SOA also decrease Ni in the tropical Pacific Ocean, the total Ni is only increased by 1.1×10^7 m^{-2} in the dbfcs_new case. The predicted Ni for each case is

compared with the observed Ni reported by *Krämer et al.* [2009] and *Krämer et al.* [2020] (Figure 5). Data from the model have been selected to have ice water mixing ratios > 10^{-8} to match values seen in the in-situ observations [*Krämer et al.*, 2016]. Whether or not our predicted SOA INP (shown in Figure 1) acts as an ice nuclei in updrafts depends on the competition with other aerosols as well as the updraft speeds. Furthermore, the ice crystal number concentration is subject to change after nucleation by aerosols due to detrainment, the Bergeron process, melting of ice, freezing of cloud drops, autoconversion from ice to snow, growth and sublimation of ice, and sedimentation of ice. As a result, the in-cloud Ni shown in Figure 5 is smaller than the grid average number concentration that may act as INPs shown in Figure 1. All simulations do a reasonable job of representing the ice crystal number concentrations for all temperatures except for the somewhat high concentrations seen between 195K and 215K. The inclusion of INPs from SOA increases Ni between 190K and 220K, but decreases Ni slightly at the lowest temperatures.

.2 Radiative effects

The change in Ni resulting from the addition of INPs from SOA changes the predicted ice water path (IWP) and effective radius, and thereby changes the radiative effects of cirrus clouds. Generally, smaller Ni due to the additional INPs from SOA leads to larger cloud ice sizes, so that the ice crystals are removed faster. As a result, the IWP decreases with the decrease in Ni and vice versa as shown by comparing Figures 4a and c, and Figures 4b and d. The decrease in the global average Ni in the dbfcs_fix case leads to a global average decrease in IWP of 0.1±0.04 g m^{-2}, while the small increase in global average Ni in the dbfcs_new case causes a decrease in IWP by 0.07±0.03 g m^{-2}. While the global average difference in IWP in these two cases is similar, the geographical changes differ. The difference in the sign of the response of IWP to changes in Ni results from the geographic distribution of IWP and the change of Ni. The IWP is much higher over the tropics (10°S~10°N) than over Antarctica (60°S~90°S) (Figure 6). Ni is increased by 18.5×10^{7} m^{-2} over Antarctica from the BASE case to the dbfcs_new case, which leads to an increase of 0.03 g m^{-2} (3.4%) in IWP over Antarctica. In comparison, although Ni is only decreased by 2.84×10^{7} m^{-2} over the tropics, the IWP

there is decreased by 0.27 g m^{-2} (1.3%), which is much larger than the IWP increase over Antarctica because of the much higher IWP (20.77 g m^{-2}) over the tropics compared to that over Antarctica (0.88 g m^{-2}) (Figure 6). In comparison, the decrease in Ni in the dbfcs_fix case causes a decrease in the IWP over both the tropics and Antarctica (Figure 4d). The decrease in IWP over the west Pacific Ocean and north Indian Ocean, where the IWP is largest (Figure 6c), still dominates the change in IWP in the dbfcs_fix case.

The changes in the short-wave (FSNT) and long-wave (FLNT) radiative fluxes follow the changes of IWP and have opposite signs (Figure 4). FSNT decreases and FLNT increases in most regions except the tropical Pacific Ocean in the dbfcs_new case compared to the BASE case. In comparison, there are additional enhancements of FSNT and reductions of FLNT in the south Indian Ocean in the dbfcs_fix case compared to the BASE case. As a result, the effect of SOA in the dbfcs_fix case on FSNT and FLNT is smaller than that of SOA in the dbfcs_new case. The total net radiative fluxes (FNT) are the sum of the changes in FSNT and FLNT. FNT is mostly determined by FLNT because the longwave cirrus radiative effect is always larger than the

shortwave cirrus radiative effect. The difference in FNT between the dbfcs_new and BASE case is 0.35±0.06 W m^{-2} (the uncertainty is the standard deviation of the interannual variation hereafter), while it is 0.31±0.08 W m^{-2} between the dbfcs_fix and BASE case. The warming effect of SOA on cirrus clouds is largest for both cases in the high-latitude regions of both the NH and SH around 70°S and 70°N as well as in the tropical regions (20°S~20°N) (Figure 7e). The effect of SOA on the increase in FLNT is much larger than that on the decrease in FSNT in these regions, except that the effect of SOA on FLNT is negative around equator and 20S for the dbfcs_fix case (Figure 7a). The effect of SOA on FSNT is negative from 30S to 20N for the dbfcs_new case, while the effect is mostly positive in these regions for the dbfcs_fix case (Figure 7c). SOA particles only cause a slight negative net radiative effect on cirrus in the regions around 30°S and 30°N for both cases that include SOA (Figure 7e). While not statistically significant, the global average net radiative effect of SOA on cirrus for the dbfcs_new case is 13% more positive than that for the dbfcs_fix case. The slightly larger radiative effect of SOA in the dbfcs_new case is primarily due to the higher positive radiative effects of the SOA in the dbfcs_new case at low-

(30°S~0°) and high-latitude (90°S~60°S) regions in the SH compared to that of SOA in the dbfcs_fix case. This is because of the larger decrease of Ni due to SOA in the dbfcs_fix case in the south Indian Ocean and the increase of Ni over Antarctica in the dbfcs_new case.

3.3 Influence on the radiative forcing of aircraft soot

The addition of INPs from SOA change the background Ni, and thereby likely have an influence on the estimation of radiative effects of other aerosol species on cirrus clouds. According to the simulations reported in *Penner et al.* [2018], the radiative forcing by contrail-processed anthropogenic aircraft soot is the largest single forcing among the forcings on cirrus caused by anthropogenic soot, which they calculated as -0.20 W m^{-2} caused by a 2.78 $\times 10^{7}$ m^{-2} decrease in the global average Ni. Therefore, we designed two experiments to study the effect of SOA on contrail-processed aircraft soot (CEX_new: dbfcs_new-dbfs_new and CEX_fix: dbfcs_fix-dbfs_fix) to evaluate the radiative forcing of aircraft soot after incorporation into contrails when the background heterogeneous INP are increased as a result of SOA acting as in INP. The INPs from aircraft soot mainly cause decreases in

the column integrated Ni which varies between -20×10^6 and -100×10^6 m^{-2} when SOA is not included (Figure 9a in *Penner et al.* [2018]), and an indirect increase of Ni in the west Pacific due to the enhancement of the Walker circulation [*Zhou and Penner*, 2014]. As shown above, INPs from SOA preclude homogeneous freezing in the north Indian Ocean similar to the effect of aircraft soot, which contributes to a decrease of Ni there (Figure 4a, 4b). As a result, the INPs from aircraft soot decrease Ni less in the north Indian Ocean after including INPs from SOA (compare Figures 8a, 8b with Figure 9a). Although a smaller cooling in the north Indian Ocean would reduce the effects of the increase of Ni in the west Pacific Ocean, the effect of aircraft soot on global average Ni is less negative after including INPs from SOA. Because the INPs from SOA in the dbfcs_fix case decrease more Ni in the north Indian Ocean than those in the dbfcs_new case (compare Figure 4a and Figure 4b), the INPs from aircraft soot decrease the global average Ni in the CEX_fix case less than that in the CEX_new case (-1.83×10^7 m^{-2} vs -2.34×10^7 m^{-2}). However, the INPs from SOA in the dbfcs_new case increase Ni in the tropical Indian Ocean in the SH, while the INPs from SOA in the dbfcs_fix case decrease Ni there (Figure 4a, 4b). This difference causes a larger increase of Ni in

the tropical Indian Ocean in the SH in the CEX_new case than that in the CEX_fix case, especially in the area off the east coast of central Africa.

The change in Ni due to contrail-processed aircraft soot contributes to the change in IWP, FSNT and FLNT as shown in Figure 8 for the cases including SOA and in Figure 9 for the case excluding SOA. The changes in ice crystal size and number have an influence on the IWP, cloud cover, lifetime and optical properties of cirrus clouds, and therefore impact the radiative forcing. Because the INPs from aircraft soot without SOA decrease Ni more, they have a larger influence on IWP, FSNT and FLNT than the INPs from aircraft soot when SOA is included as an INP, and therefore result in a larger negative radiative forcing (-0.20 W m^{-2}) than the radiative forcing of aircraft soot in the CEX_new (-0.11±0.03 W m^{-2}) and CEX_fix (-0.16±0.02 W m^{-2}) cases. The zonal average FNT due to contrail-processed aircraft soot when SOA is included is similar for the two cases, except in low-latitude regions of the SH (30°S~10°S) (Figure 7f). The difference in FNT in this region is caused by the difference in the change of Ni due to aircraft soot between CEX_new and CEX_fix. The effect of aircraft soot on the IWP in these low-latitude regions in the SH in CEX_new is positive or less negative than that in CEX_fix. The

different effects on IWP lead to a positive or less negative FNT in that region in the CEX_new case compared to that in the CEX_fix case. As a result, the global average radiative forcing of aircraft soot on cirrus is 31% less negative in CEX_new than that in CEX_fix.

3.4 Historical radiative forcing of SOA

Changes in climate and land use cause changes to the emissions of SOA precursors from the PI to the present day (PD) [*Zhu et al.*, 2019], thereby changing the number concentration of newly formed SOA as well as the INPs from SOA. We designed two experiments to evaluate the radiative forcing of cirrus clouds due to the changes in SOA from the PI to the PD (RF_new: dbfcs_new-dbfcs_PI_new and RF_fix: dbfcs_fix-dbfcs_PI_fix). As shown in Figure 10, the difference in the number concentration of INPs from SOA between the PD and PI simulations have different signs due to the different SOA treatments of size distribution. The global average emissions of the precursors of SOA (i.e. isoprene, α-pinene and limonene in this model) in both experiments decrease between the PD and PI simulations due to the combined effect of climate and land use change [*Zhu et al.*, 2019], resulting in a decrease in the burden of SOA between the PD and PI simulations. As a result, the

number concentration of INPs from SOA decreases due to the decrease in the burden of total SOA between the PD and PI simulations when using the assumed size distribution in RF_fix (Figure 10c, 10d). However, the anthropogenic emissions of sulfur in the PD (55 Tg S $year^{-1}$) are much larger than those in the PI atmosphere (2.2 Tg S $year^{-1}$). Sulfuric acid as well as water condense on the newSOA particles after the formation of new particles, and are responsible for most of the growth of small newSOA particles to the accumulation mode [*Zhu and Penner*, 2019]. As a result, the number concentration of newSOA in the accumulation mode is much higher in the PD compared to the PI atmosphere. So even though the mass concentration of SOA is decreased, the number concentration of INPs from SOA is increased between the PD and PI simulations when using the calculated size distribution of newly formed SOA in RF_new (Figure 10a, 10b and *Zhu et al.*, 2019), which is opposite to that in the RF_fix experiment.

The differences in the change of INPs from SOA in the two experiments leads to a difference in the change in Ni. In the RF_new experiment, the increase in the INPs from SOA causes a large increase in the Ni from heterogeneous nucleation, which precludes the occurrence of

homogeneous nucleation (Figure 11a, 11c). The increase in the Ni from heterogeneous nucleation outweighs the decrease in the Ni from homogeneous nucleation, leading to the increase of 0.68×10^{8} m^{-2} in the global average Ni due to the increase in the SOA in the RF_new experiment (Figure 12a). In contrast, the decrease in the INPs from SOA in the RF_fix experiment reduces heterogeneous nucleation and somewhat increases the Ni from homogeneous nucleation (Figure 11b, 11d). The change in the heterogeneous nucleation due to the decrease in the SOA also dominates the change in Ni in the RF_fix experiment, so that the global average Ni is decreased by 0.11×10^{8} m^{-2} in the RF_fix experiment which has the opposite sign of the change of Ni in the RF_new experiment (Figure 12b). The difference in the change of Ni between RF_new and RF_fix causes a difference in the spatial distribution of the change in the IWP. The IWP increases in the north Indian Ocean as well as over Antarctica and decreases over the west Pacific Ocean in the RF_new experiment, while the IWP decreases over the north Indian Ocean and increases over the west Pacific Ocean in the RF_fix experiment (Figure 12c, 12d). The changes in the FSNT and FLNT also have different signs in two experiments due to the different

treatments of the SOA size distribution. In the RF_new experiment, the increase in the INP number concentration from SOA contributes to the decrease in the global average FSNT and increase in the global average FLNT, which are dominated by the changes over the north Indian Ocean (Figure 12e, 12g). On the other hand, the decrease in INPs from SOA in the RF_fix experiment leads to an increase in FSNT and a decrease in FLNT (Figure 12f, 12h). The net radiative changes (FNT) are dominated by the changes in FLNT compared to those in FSNT in two experiments, although there are some locations where the changes in FSNT dominate the changes in the FLNT (Figure 12). As a result, the changes in the SOA from PI to PD cause a radiative forcing in cirrus clouds with different signs in the two experiments. In the RF_new experiment, the radiative forcing on cirrus clouds due to the change of SOA is 0.02±0.04 W m^{-2}, which is attributed to the positive net forcing in the south tropics and polar regions (Figure 13). However, the change of SOA in the RF_fix experiments results in a negative forcing in the south tropics and polar regions, which leads to a global average radiative forcing of -0.03±0.05 W/m^2.

4. Conclusion and discussion

We used the CESM/IMPACT model to exam the indirect radiative effects of SOA on cirrus clouds using two treatments for the size distribution of SOA. The differences for all simulations performed here are summarized in Table 2. SOA in the accumulation mode from newly formed particles as a result of organic nucleation increases the global average Ni by 1.1×10^{7} m^{-2}, while the SOA from an assumed, fixed size distribution decreases the global average Ni by 5.5×10^{7} m^{-2}. As a result, the radiative effect of SOA from newly formed particles by organic nucleation on cirrus is 0.35±0.06 W m^{-2}, which is 13% more positive than that of SOA using a fixed size distribution (0.31±0.08 W m^{-2}). *Penner et al.* [2018] estimated the radiative forcing of aircraft soot, fossil/bio-fuel soot and biomass burning soot as -0.2, -0.093 and -0.057 W m^{-2} respectively. The radiative forcing of aircraft soot decreased to -0.1 W m^{-2} when 30% of the SOA was treated as an INP (in an external mixture), but this simulation did not include newly formed SOA particles from organic nucleation. The primary impact of including SOA is to change the background Ni for estimating the radiative forcing of other aerosols. The radiative forcing of aircraft soot is expected to decrease (become less

negative than that in *Penner et al.* [2018]) to -0.11±0.03 W m^{-2} using the predicted size distribution for newly formed SOA. The radiative forcing on cirrus clouds due to the change in the SOA between the PD and PI simulations is estimated to have different signs using the two different SOA treatments of size distribution, namely 0.02±0.04 W m^{-2} with the predicted size distribution and -0.03±0.05 W m^{-2} with the assumed fixed size distribution. Therefore, an assumed fixed size distribution should not be used for calculations that include the effect of the changes in SOA.

The calculation of the radiative effect of SOA on cirrus presented here is limited by the knowledge of the ability of SOA to act as an INP. The temperature at which SOA-containing particles form ice is uncertain since it is probably dependent on the chemical composition, particle size and mixing stat e of SOA [*Baustian et al.*, 2013; *Berkemeier et al.*, 2014; *Charnawskas et al.*, 2017], which were not considered in the model. A better quantification of the role of different organic functional groups in ice formation is needed to improve the estimation of the number concentration of INPs from SOA and its radiative effects. In addition, SOA is able to change the ability of other aerosol particles like dust and soot to form ice crystals if SOA coats those

particles [*Koehler et al.*, 2010; *Kulkarni et al.*, 2016; *Möhler et al.*, 2008]. The radiative effects of SOA on cirrus clouds may change when considering the effect of internal mixing with $(NH_4)_2SO_4$ on ice formation.

Acknowledgments

We are grateful to the reviewers and for funding from NSF-GEO grant number 1540954 and National Natural Science Foundation of China (Grant 41625014). Computer time was provided by the NCAR CISL. The updated CESM/IMPACT model and all model results used in this paper are archived at http://doi.org/ 10.7302/aqa1-5t49.

References

Abbatt, J., S. Benz, D. Cziczo, Z. Kanji, U. Lohmann, and O. Möhler (2006), Solid ammonium sulfate aerosols as ice nuclei: A pathway for cirrus cloud formation, *Science, 313*(5794), 1770-1773.

Baustian, K. J., M. E. Wise, E. J. Jensen, G. P. Schill, M. A. Freedman, and M. A. Tolbert (2013), State transformations and ice nucleation in amorphous (semi-)solid organic aerosol, *Atmospheric Chemistry and Physics*, *13*(11), 5615-5628, doi:10.5194/acp-13-5615-2013.

Berkemeier, T., M. Shiraiwa, U. Pöschl, and T. Koop (2014), Competition between water uptake and ice nucleation by glassy organic aerosol particles, *Atmospheric Chemistry and Physics*, *14*(22), 12513-12531, doi:10.5194/acp-14-12513-2014.

Cahill, J. F., K. Suski, J. H. Seinfeld, R. A. Zaveri, and K. A. Prather (2012), The mixing state of carbonaceous aerosol particles in northern and southern California measured during CARES and CalNex 2010, *Atmospheric Chemistry and Physics*, *12*(22), 10989-11002, doi:10.5194/acp-12-10989-2012.

Charnawskas, J. C., et al. (2017), Condensed-phase biogenic-anthropogenic interactions with implications for cold cloud formation, *Faraday Discuss*, *200*, 165-194, doi:10.1039/c7fd00010c.

Chen, Y., S. M. Kreidenweis, L. M. McInnes, D. C. Rogers, and P. J. DeMott (1998), Single particle analyses of ice nucleating aerosols in the upper troposphere and lower stratosphere, *Geophysical research letters*, *25*(9), 1391-1394.

Cziczo, D. J., K. D. Froyd, C. Hoose, E. J. Jensen, M. Diao, M. A. Zondlo, J. B. Smith, C. H. Twohy, and D. M. Murphy (2013), Clarifying the dominant sources and mechanisms of cirrus cloud formation, *Science*, *340*(6138), 1320-1324.

Cziczo, D. J., D. M. Murphy, P. K. Hudson, and D. S. Thomson (2004), Single particle measurements of the chemical composition of cirrus ice residue during CRYSTAL-FACE, *Journal of Geophysical Research-Atmospheres*, *109*(D4), doi:10.1029/2003jd004032.

DeMott, P., D. Cziczo, A. Prenni, D. Murphy, S. Kreidenweis, D. Thomson, R. Borys, and D. Rogers (2003), Measurements of the concentration and composition of nuclei for cirrus formation, *Proceedings of the National Academy of Sciences*, *100*(25), 14655-14660.

DeMott, P. J., A. J. Prenni, X. Liu, S. M. Kreidenweis, M. D. Petters, C. H. Twohy, M. S. Richardson, T. Eidhammer, and D. C. Rogers (2010), Predicting global atmospheric ice nuclei distributions and their impacts on climate, *Proc Natl Acad Sci U S A*, *107*(25), 11217-11222, doi:10.1073/pnas.0910818107.

Dentener, F., S. Kinne, T. Bond, O. Boucher, J. Cofala, S. Generoso, P. Ginoux, S. Gong, J. Hoelzemann, and A. Ito (2006), Emissions of primary aerosol and precursor gases in the years 2000 and 1750 prescribed data-sets for AeroCom, *Atmospheric Chemistry and Physics*, *6*(12), 4321-4344.

Froyd, K., D. Murphy, P. Lawson, D. Baumgardner, and R. Herman (2010), Aerosols that form subvisible cirrus at the tropical tropopause, *Atmospheric Chemistry and Physics*, *10*(1), 209-218.

Gary, B. L. (2006), Mesoscale temperature fluctuations in the stratosphere, *Atmospheric Chemistry and Physics*, *6*(12), 4577-4589.

Gary, B. L. (2008), Mesoscale temperature fluctuations in the Southern Hemisphere stratosphere, *Atmospheric Chemistry and Physics*, *8*(16), 4677-4681.

Gettelman, A., X. Liu, S. J. Ghan, H. Morrison, S. Park, A. Conley, S. A. Klein, J. Boyle, D. Mitchell, and J. L. Li (2010), Global simulations of ice nucleation and ice supersaturation with an improved cloud scheme in the Community Atmosphere Model, *Journal of Geophysical Research: Atmospheres*, *115*(D18).

Gong, S., L. Barrie, and J. P. Blanchet (1997), Modeling sea - salt aerosols in the atmosphere: 1. Model development, *Journal of Geophysical Research: Atmospheres*, *102*(D3), 3805-3818.

Gordon, H., et al. (2016), Reduced anthropogenic aerosol radiative forcing caused by biogenic new particle formation, *Proc Natl Acad Sci U S A*, *113*(43), 12053-12058, doi:10.1073/pnas.1602360113.

Hoose, C., and O. Möhler (2012), Heterogeneous ice nucleation on atmospheric aerosols: a review of results from laboratory experiments, *Atmospheric Chemistry and Physics*, *12*(20), 9817-9854, doi:10.5194/acp-12-9817-2012.

Ignatius, K., et al. (2016), Heterogeneous ice nucleation of viscous secondary organic aerosol produced from ozonolysis of alpha-pinene, *Atmospheric Chemistry and Physics*, *16*(10), 6495-6509, doi:10.5194/acp-16-6495-2016.

Kärcher, B., J. Hendricks, and U. Lohmann (2006), Physically based parameterization of cirrus cloud formation for use in global atmospheric models, *Journal of Geophysical Research*, *111*(D1), doi:10.1029/2005jd006219.

Kärcher, B., and J. Ström (2003), The roles of dynamical variability and aerosols in cirrus cloud formation, *Atmospheric Chemistry and Physics*, *3*(3), 823-838.

Kirkby, J., et al. (2016), Ion-induced nucleation of pure biogenic particles, *Nature*, *533*(7604), 521-526, doi:10.1038/nature17953.

Knopf, D. A., P. A. Alpert, and B. Wang (2018), The Role of Organic Aerosol in Atmospheric Ice Nucleation: A Review, *ACS Earth and Space Chemistry*, *2*(3), 168-202, doi:10.1021/acsearthspacechem.7b00120.

Koehler, K. A., P. J. DeMott, S. M. Kreidenweis, O. B. Popovicheva, M. D. Petters, C. M. Carrico, E. D. Kireeva, T. D. Khokhlova, and N. K. Shonija (2009), Cloud condensation nuclei and ice nucleation activity of hydrophobic and hydrophilic soot particles, *Physical Chemistry Chemical Physics*, *11*(36), 7906-7920.

Koehler, K. A., S. M. Kreidenweis, P. J. DeMott, M. D. Petters, A. J. Prenni, and O. Möhler (2010), Laboratory investigations of the impact of

mineral dust aerosol on cold cloud formation, *Atmospheric Chemistry and Physics*, *10*(23), 11955-11968, doi:10.5194/acp-10-11955-2010.

Koop, T., J. Bookhold, M. Shiraiwa, and U. Poschl (2011), Glass transition and phase state of organic compounds: dependency on molecular properties and implications for secondary organic aerosols in the atmosphere, *Phys Chem Chem Phys*, *13*(43), 19238-19255, doi:10.1039/c1cp22617g.

Koop, T., B. P. Luo, A. Tsias, and T. Peter (2000), Water activity as the determinant for homogeneous ice nucleation in aqueous solutions, *Nature*, *406*(6796), 611-614, doi:10.1038/35020537.

Koop, T., H. P. Ng, L. T. Molina, and M. J. Molina (1998), A new optical technique to study aerosol phase transitions: The nucleation of ice from H2SO4 aerosols, *J. Phys. Chem. A*, *102*(45), 8924-8931, doi:10.1021/jp9828078.

Krämer, M., C. Rolf, A. Luebke, A. Afchine, N. Spelten, A. Costa, J. Meyer, M. Zoeger, J. Smith, and R. L. Herman (2016), A microphysics guide to cirrus clouds-Part 1: Cirrus types, *Atmospheric Chemistry and Physics*, *16*, 3463-3483.

Krämer, M., C. Rolf, N. Spelten, A. Afchine, D. Fahey, E. Jensen, S. Khaykin, T. Kuhn, P. Lawson, and A. Lykov (2020), A Microphysics Guide to Cirrus–Part II: Climatologies of Clouds and Humidity from Observations, *Atmospheric Chemistry and Physics Discussions*, doi:10.5194/acp-2020-40.

Krämer, M., C. Schiller, A. Afchine, R. Bauer, I. Gensch, A. Mangold, S. Schlicht, N. Spelten, N. Sitnikov, and S. Borrmann (2009), Ice supersaturations and cirrus cloud crystal numbers, *Atmospheric Chemistry and Physics*, *9*(11), 3505-3522.

Kulkarni, G., et al. (2016), Ice nucleation activity of diesel soot particles at cirrus relevant temperature conditions: Effects of hydration, secondary organics coating, soot morphology, and coagulation, *Geophysical Research Letters*, *43*(7), 3580-3588, doi:10.1002/2016gl068707.

Lamarque, J. F., et al. (2012), CAM-chem: description and evaluation of interactive atmospheric chemistry in the Community Earth System Model, *Geoscientific Model Development*, *5*(2), 369-411, doi:10.5194/gmd-5-369-2012.

Li, J. L. F., et al. (2012), An observationally based evaluation of cloud ice water in CMIP3 and CMIP5 GCMs and contemporary reanalyses using

contemporary satellite data, *Journal of Geophysical Research-Atmospheres*, *117*, doi:10.1029/2012jd017640.

Lin, G., J. E. Penner, S. Sillman, D. Taraborrelli, and J. Lelieveld (2012), Global modeling of SOA formation from dicarbonyls, epoxides, organic nitrates and peroxides, *Atmospheric Chemistry and Physics*, *12*(10), 4743-4774, doi:10.5194/acp-12-4743-2012.

Lin, G., S. Sillman, J. E. Penner, and A. Ito (2014), Global modeling of SOA: the use of different mechanisms for aqueous-phase formation, *Atmospheric Chemistry and Physics*, *14*(11), 5451-5475, doi:10.5194/acp-14-5451-2014.

Mårtensson, E., E. Nilsson, G. de Leeuw, L. Cohen, and H. C. Hansson (2003), Laboratory simulations and parameterization of the primary marine aerosol production, *Journal of Geophysical Research: Atmospheres*, *108*(D9).

Möhler, O., S. Benz, H. Saathoff, M. Schnaiter, R. Wagner, J. Schneider, S. Walter, V. Ebert, and S. Wagner (2008), The effect of organic coating on the heterogeneous ice nucleation efficiency of mineral dust aerosols, *Environmental Research Letters*, *3*(2), 025007, doi:10.1088/1748-9326/3/2/025007.

Morrison, H., and A. Gettelman (2008), A new two-moment bulk stratiform cloud microphysics scheme in the Community Atmosphere Model, version 3 (CAM3). Part I: Description and numerical tests, *Journal of Climate*, *21*(15), 3642-3659.

Murray, B. J., et al. (2010), Heterogeneous nucleation of ice particles on glassy aerosols under cirrus conditions, *Nature Geoscience*, *3*(4), 233-237, doi:10.1038/ngeo817.

Pajunoja, A., J. Malila, L. Q. Hao, J. Joutsensaari, K. E. J. Lehtinen, and A. Virtanen (2014), Estimating the Viscosity Range of SOA Particles Based on Their Coalescence Time, *Aerosol Sci. Technol.*, *48*(2), I-IV, doi:10.1080/02786826.2013.870325.

Penner, J. E., C. Zhou, A. Garnier, and D. L. Mitchell (2018), Anthropogenic Aerosol Indirect Effects in Cirrus Clouds, *Journal of Geophysical Research: Atmospheres*, *123*(20), 11,652-611,677, doi:10.1029/2018jd029204.

Podglajen, A., A. Hertzog, R. Plougonven, and B. Legras (2016), Lagrangian temperature and vertical velocity fluctuations due to gravity waves in the lower stratosphere, *Geophysical Research Letters*, *43*(7), 3543-3553.

Pratt, K., S. Murphy, R. Subramanian, P. DeMott, G. Kok, T. Campos, D. Rogers, A. Prenni, A. Heymsfield, and J. Seinfeld (2011), Flight-based chemical characterization of biomass burning aerosols within two prescribed burn smoke plumes, *Atmospheric Chemistry and Physics*, *11*(24), 12549-12565.

Pratt, K. A., and K. A. Prather (2010), Aircraft measurements of vertical profiles of aerosol mixing states, *Journal of Geophysical Research*, *115*(D11), doi:10.1029/2009jd013150.

Pusechel, R., D. Blake, K. Snetsinger, A. Hansen, S. Verma, and K. Kato (1992), Black carbon (soot) aerosol in the lower stratosphere and upper troposphere, *Geophysical research letters*, *19*(16), 1659-1662.

Renbaum-Wolff, L., J. W. Grayson, A. P. Bateman, M. Kuwata, M. Sellier, B. J. Murray, J. E. Shilling, S. T. Martin, and A. K. Bertram (2013), Viscosity of alpha-pinene secondary organic material and implications for particle growth and reactivity, *Proc. Natl. Acad. Sci. U. S. A.*, *110*(20), 8014-8019, doi:10.1073/pnas.1219548110.

Riccobono, F., et al. (2014), Oxidation products of biogenic emissions contribute to nucleation of atmospheric particles, *Science*, *344*(6185), 717-721, doi:10.1126/science.1243527.

Richardson, M. S., et al. (2007), Measurements of heterogeneous ice nuclei in the western United States in springtime and their relation to aerosol characteristics, *Journal of Geophysical Research-Atmospheres*, *112*(D2), doi:10.1029/2006jd007500.

Satheesh, S. K., and K. K. Moorthy (2005), Radiative effects of natural aerosols: A review, *Atmospheric Environment*, *39*(11), 2089-2110, doi:10.1016/j.atmosenv.2004.12.029.

Saukko, E., et al. (2012), Humidity-dependent phase state of SOA particles from biogenic and anthropogenic precursors, *Atmospheric Chemistry and Physics*, *12*(16), 7517-7529, doi:10.5194/acp-12-7517-2012.

Shiraiwa, M., Y. Li, A. P. Tsimpidi, V. A. Karydis, T. Berkemeier, S. N. Pandis, J. Lelieveld, T. Koop, and U. Pöschl (2017), Global distribution of particle phase state in atmospheric secondary organic aerosols, *Nature Communications*, *8*, 15002, doi:10.1038/ncomms15002.

Spichtinger, P., and D. J. Cziczo (2010), Impact of heterogeneous ice nuclei on homogeneous freezing events in cirrus clouds, *Journal of Geophysical Research-Atmospheres*, *115*, doi:10.1029/2009jd012168.

van der Werf, G. R., J. T. Randerson, L. Giglio, G. J. Collatz, P. S. Kasibhatla, and A. F. Arellano Jr (2006), Interannual variability in global biomass burning emissions from 1997 to 2004, *Atmospheric Chemistry and Physics*, *6*(11), 3423-3441.

Wagner, R., et al. (2017), Heterogeneous ice nucleation of α-pinene SOA particles before and after ice cloud processing, *Journal of Geophysical Research: Atmospheres*, *122*(9), 4924-4943, doi:10.1002/2016jd026401.

Wang, B., A. T. Lambe, P. Massoli, T. B. Onasch, P. Davidovits, D. R. Worsnop, and D. A. Knopf (2012), The deposition ice nucleation and immersion freezing potential of amorphous secondary organic aerosol: Pathways for ice and mixed - phase cloud formation, *Journal of Geophysical Research: Atmospheres*, *117*(D16).

Wang, M., and J. E. Penner (2010), Cirrus clouds in a global climate model with a statistical cirrus cloud scheme, *Atmospheric Chemistry and Physics*, *10*(12), 5449-5474, doi:10.5194/acp-10-5449-2010.

Welti, A., F. Luond, O. Stetzer, and U. Lohmann (2009), Influence of particle size on the ice nucleating ability of mineral dusts, *Atmospheric Chemistry and Physics*, *9*(18), 6705-6715, doi:10.5194/acp-9-6705-2009.

Wilson, T. W., et al. (2012), Glassy aerosols with a range of compositions nucleate ice heterogeneously at cirrus temperatures, *Atmospheric Chemistry and Physics*, *12*(18), 8611-8632, doi:10.5194/acp-12-8611-2012.

Zender, C. S., H. Bian, and D. Newman (2003), Mineral Dust Entrainment and Deposition (DEAD) model: Description and 1990s dust climatology, *Journal of Geophysical Research: Atmospheres*, *108*(D14).

Zhang, K., H. Wan, X. Liu, S. J. Ghan, G. J. Kooperman, P.-L. Ma, P. J. Rasch, D. Neubauer, and U. Lohmann (2014), On the use of nudging for aerosol–climate model intercomparison studies, *Atmospheric Chemistry and Physics*, *14*(16), 8631-8645.

Zhao, B., Y. Wang, Y. Gu, K. N. Liou, J. H. Jiang, J. Fan, X. Liu, L. Huang, and Y. L. Yung (2019), Ice nucleation by aerosols from anthropogenic pollution, *Nat Geosci*, *12*, 602-607, doi:10.1038/s41561-019-0389-4.

Zhou, C., and J. E. Penner (2014), Aircraft soot indirect effect on large-scale cirrus clouds: Is the indirect forcing by aircraft soot positive or negative?, *Journal of Geophysical Research-Atmospheres*, *119*(19), 11303-11320, doi:10.1002/2014jd021914.

Zhou, C., J. E. Penner, G. Lin, X. Liu, and M. Wang (2016), What controls the low ice number concentration in the upper troposphere?, *Atmospheric Chemistry and Physics*, *16*(19), 12411-12424, doi:10.5194/acp-16-12411-2016.

Zhu, J., and J. E. Penner (2019), Global Modeling of Secondary Organic Aerosol With Organic Nucleation, *Journal of Geophysical Research: Atmospheres*, *124*(14), 8260-8286.

Zhu, J., J. E. Penner, G. Lin, C. Zhou, L. Xu, and B. Zhuang (2017), Mechanism of SOA formation determines magnitude of radiative effects, *Proc Natl Acad Sci U S A*, *114*(48), 12685-12690, doi:10.1073/pnas.1712273114.

Zhu, J., J. E. Penner, F. Yu, S. Sillman, M. O. Andreae, and H. Coe (2019), Decrease in radiative forcing by organic aerosol nucleation, climate, and land use change, *Nature Communications*, *10*(1), 423, doi:10.1038/s41467-019-08407-7.

Figure captions

Figure 1. The vertically integrated number (m^{-2}) (a, c) and zonal average number concentration (L^{-1}) (b,d) plots of SOA that are available to act as INPs in the Kärcher et al. (2006) parameterization in the s_new scheme (a, b) and s_fix scheme (c, d).

Figure 2. Percentage of ice crystal number concentration formed from homogeneous freezing for the dbfc (a), dbfcs_new (b), and dbfcs_fix (c) cases and the difference between the dbfcs_new and dbfc cases (d) as well as the difference between the dbfcs_fix and dbfc cases (e).

Figure 3. The difference of vertically integrated number concentration (m^{-2}) of new ice formed from homogeneous (a, b) and heterogeneous (c, d) freezing between dbfcs_new and dbfc cases (a, c) as well as between the dbfcs_fix and dbfc cases (b, d).

Figure 4. Annual mean plots of the change in vertically integrated average ice crystal number concentration (m^{-2}) (a, b) and vertically

integrated ice water path (g m^{-2}) (c, d) as well as net incoming shortwave radiation (W m^{-2}) (e, f), long wave radiation (W m^{-2}) (g, h) and net radiation (W m^{-2}) (i, j) for the difference between the dbfcs_new and dbfc cases (a, c, e, g, i) and the dbfcs_fix and dbfc cases (b, d, f, h, j).

Figure 5. In-cloud ice crystal number concentration (L^{-1}) versus temperature (K) for the dbfc (purple line), dbfcs_new (red line) and dbfcs_fix (green line) cases with error bars of 25th and 75th percentiles. The background shaded region shows the 25th-75th percentiles from an extended set of observations originally compiled by *Krämer et al.* [2009].

Figure 6. The annual mean ice water path (g m^{-2}) in the dbfc (a), dbfcs_new (b) and dbfcs_fix (c) cases. We note that the global average IWP is 13.8~13.9 g m^{-2}, which is lower than that observed in different CloudSat/CALIPSO analyses (21~28 g m^{-2}) [*Li et al.*, 2012]. We used a cut off diameter of 250 μm to move cloud ice to snow. A cutoff diameter of 400 μm in the model almost doubles the IWP (compare IWP of dbfc_mg10 and dbfc in Table 3 in Penner et al., 2018).

Figure 7. Change in longwave effects (ΔFLNT, a, b), shortwave effects (ΔFSNT, c, d) and net effects (ΔFNT, e, f) at the top-of-the-atmosphere for the difference between the dbfcs_new and dbfc cases (a, c, e, red line), the dbfcs_fix and dbfc cases (a, c, e, blue line). Change in longwave forcing, shortwave forcing, and net forcing by contrail-processed aircraft soot from the difference in the dbfcs_new and dbfs_new cases (b, d, f, red line) as well as the dbfcs_fix and dbfs_fix cases (b, d, f, blue line). The shading represents one standard deviation of the interannual variation over six years.

Figure 8. Annual mean plots of the change in vertically integrated averaged ice crystal number concentration (m^{-2}) (a, b) and vertically integrated ice water path (g m^{-2}) (c, d) as well as shortwave forcing (W m^{-2}) (e, f), long wave forcing (W m^{-2}) (g, h) and net forcing (W m^{-2}) (i, j) after adding contrail-processed aircraft soot (the difference between the dbfcs_new and dbfs_new cases (a, c, e, g, i) and the dbfcs_fix and dbfs_fix cases (b, d, f, h, j)).

Figure 9. Annual mean plots of the change in grid box averaged ice crystal number concentration (m^{-2}) (a) and vertically integrated ice water path (g m^{-2}) (b) as well as shortwave forcing (W m^{-2}) (c), long wave forcing (W m^{-2}) (d) and net forcing (W m^{-2}) (e) after adding contrail-processed aircraft soot as INP excluding SOA as INP as in *Penner et al.* [2018] (replotted from Figure 9a in *Penner et al.* [2018]).

Figure 10. The vertically integrated number of INP (m^{-2}) (a, c) and zonal average plots of INP (L^{-1}) (b, d) from SOA for the difference between between the dbfcs_new and dbfcs_PI_new cases (a, b) and the dbfcs_fix and dbfcs_PI_fix cases (c, d).

Figure 11. The difference of vertically integrated number concentration (m^{-2}) of new ice formed from homogeneous (a, b) and heterogeneous (c, d) freezing between dbfcs_new and dbfcs_PI_new cases (a, c) as well as between the dbfcs_fix and dbfcs_PI_fix cases (b, d).

Figure 12. Annual mean plots of the change in vertically integrated averaged ice crystal number concentration (m^{-2}) (a, b) and vertically integrated ice water path (g m^{-2}) (c, d) as well as shortwave forcing (W m^{-2}) (e, f), long wave forcing (W m^{-2}) (g, h) and net forcing (W m^{-2}) (i, j) for the difference between the dbfcs_new and dbfcs_PI_new cases (a, c, e, g, i) and the dbfcs_fix and dbfcs_PI_fix cases (b, d, f, h, j).

Figure 13. Change in longwave forcing (ΔFLNT, a), shortwave forcing (ΔFSNT, b) and net forcing (ΔFNT, c) for the difference between the dbfcs_new and dbfcs_PI_new cases (red line) as well as the dbfcs_fix and dbfsc_PI_fix cases (blue line). The shading is one standard deviation of interannual variation over six years.

Table

Table 1 Description of cases

Case name	Description
dbfc or BASE	Emission for the present day for anthropogenic sulfur, dust, biomass soot, fossil fuel soot and aircraft soot incorporated into contrails
dbfcs_new	As in dbfc, but adding INPs from newly formed SOA particles for the present day
dbfcs_fix	As in dbfc, but adding INPs from SOA with an assumed size distribution for the present day
dbfs_new	As in dbfcs_new but without INPs from aircraft soot incorporated into contrails
dbfs_fix	As in dbfcs_fix but without INPs from aircraft soot incorporated into contrails
dbfcs_PI_new	As in dbfcs_new, but using SOA in the preindustrial period
dbfcs_PI_fix	As in dbfcs_fix, but using SOA in the preindustrial period
CEX_new	The difference between dbfcs_new and dbfs_new
CEX_fix	The difference between dbfcs_fix and dbfs_fix
RF_new	The difference between dbfcs_new and dbfcs_PI_new
RF_fix	The difference between dbfcs_fix and dbfcs_PI_fix

Note: SOA=secondary organic aerosol; INP=ice nucleating particle

Table 2 Changes in ice crystal number concentration (Ni), ice water path (IWP) as well as shortwave radiative effects (FSNT), longwave radiative effects (FLNT) and net radiative effect (FNT) for the difference between dbfcs_new and dbfc or the difference between dbfcs_fix and dbfc or CEX_new or CEX_fix or RF_new or RF_fix.

	Ni (10^7 m^{-2})	IWP (g m^{-2})	FSNT (W m^{-2})	FLNT (W m^{-2})	FNT (W m^{-2})
dfbcs_new-dfbc	1.11	-0.07	-0.27	0.62	0.35
dfbcs_fix-dfbc	-5.45	-0.10	-0.01	0.33	0.31
CEX_new	-2.34	-0.17	0.32	-0.43	-0.11
CEX_fix	-1.83	-0.16	0.31	-0.47	-0.16
RF_new	6.79	0.03	-0.25	0.27	0.02
RF_fix	-1.08	0.02	0.04	-0.07	-0.03

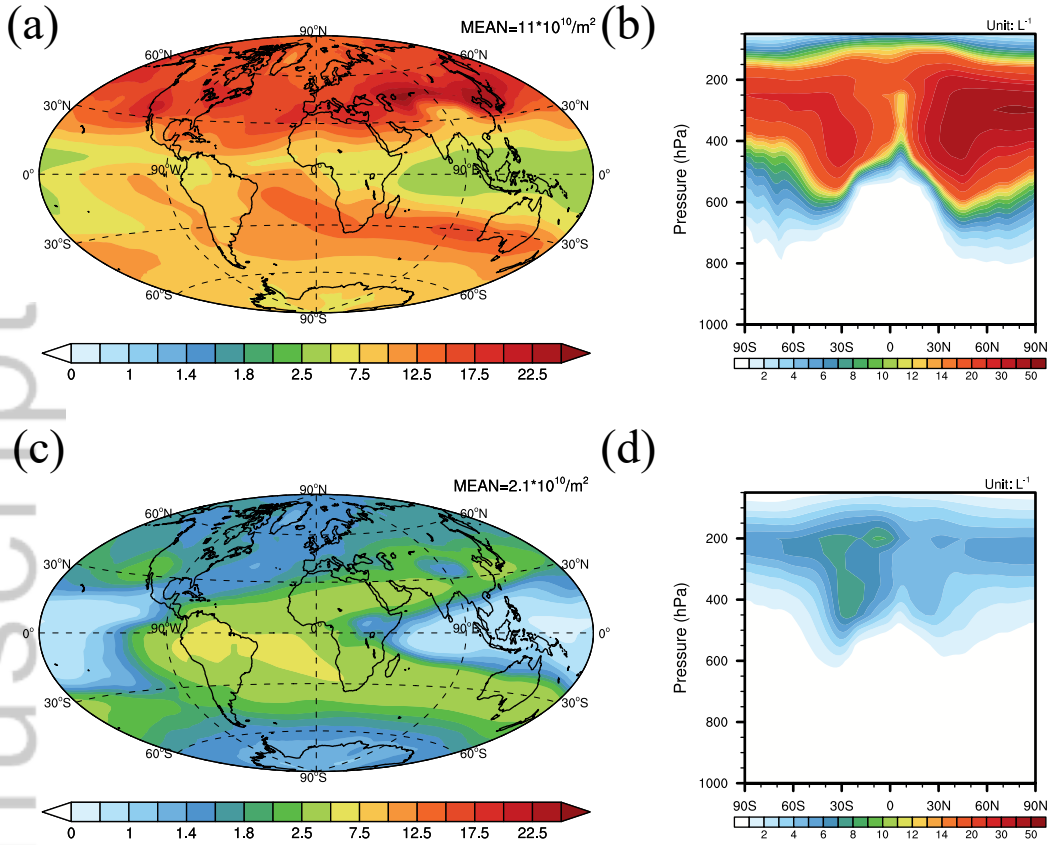

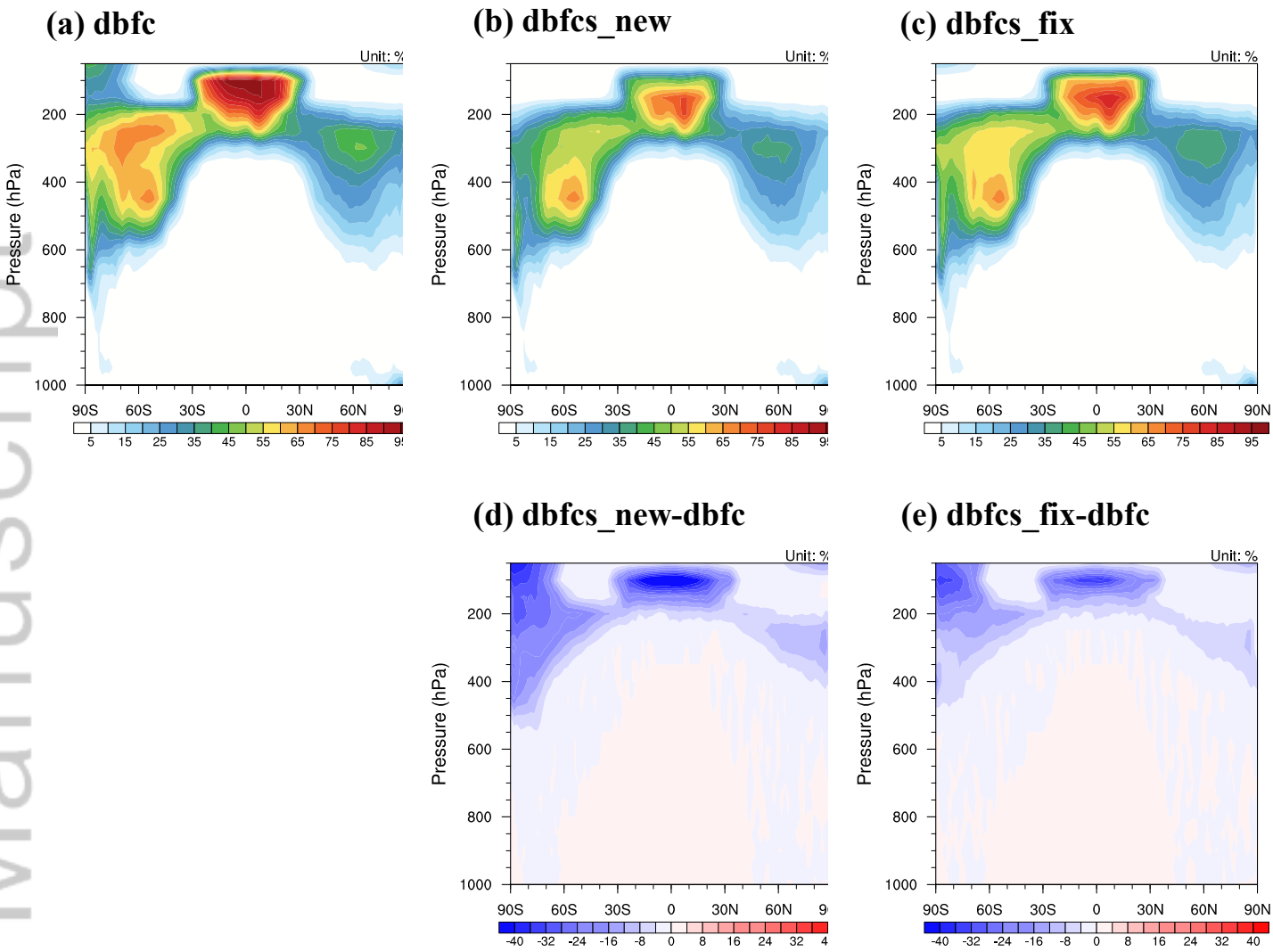

(a) dbfcs_new-dbfc

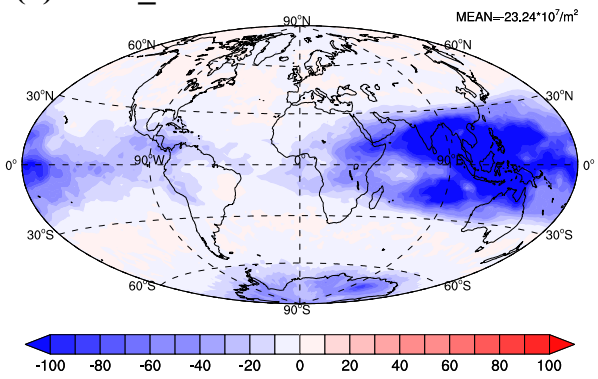

(b) dbfcs_fix-dbfc

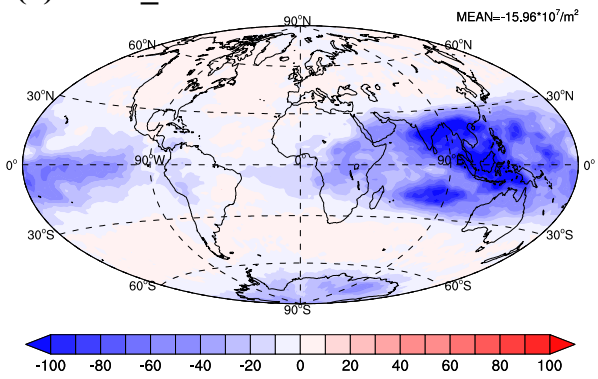

(c) dbfcs_new-dbfc

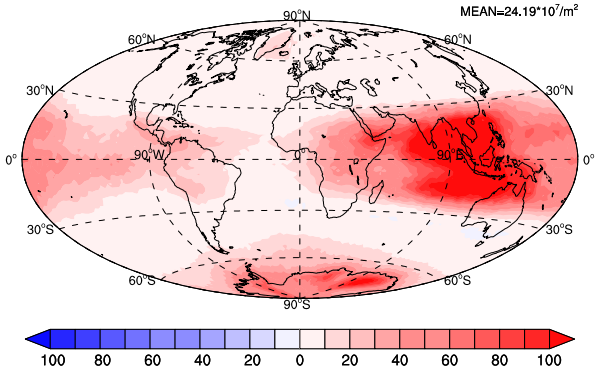

(d) dbfcs_fix-dbfc